High-order harmonic generation in a strongly overdriven regime

B. Major [1,2] K. Kovács [3,*] E. Svirplys [4] M. Anus [4] O. Ghafur,[4] K. Varjú [1,2]
M. J. J. Vrakking,[4] V. Tosa [3] and B. Schütte [4,†]

[1]*ELI-ALPS, ELI-HU Non-Profit Ltd., Wolfgang Sandner utca 3, Szeged 6728, Hungary*
[2]*Department of Optics and Quantum Electronics, University of Szeged, Dóm Tér 9, Szeged 6720, Hungary*
[3]*National Institute for Research and Development of Isotopic and Molecular Technologies,*
Donat Street 67-103, 400293 Cluj-Napoca, Romania
[4]*Max-Born-Institut, Max-Born-Strasse 2A, 12489 Berlin, Germany*

High-order harmonic generation (HHG) normally requires a careful adjustment of the driving laser intensity (typically 10^{14}–10^{15} W/cm^2) and gas medium parameters to obtain a microscopically and macroscopically optimized output. In contrast to conventional wisdom, we present experimental results indicating efficient HHG in all rare gases, using a high-density medium and a driving laser intensity of around 10^{16} W/cm^2. The experimental results are corroborated by theoretical simulations, which indicate that ionization-induced self-phase modulation and plasma defocusing self-regulate the driver laser intensity to a level that allows efficient HHG. A tenfold broadening of the driving near-infrared spectrum is observed, which results in the generation of continuous spectra from 18 to 140 eV in spite of using 50-fs-long driving pulses. The presented scheme represents a simple and versatile concept for the generation of extreme-ultraviolet and soft-x-ray continua, which could be used for transient absorption and reflection spectroscopy.

I. INTRODUCTION

In high-order harmonic generation (HHG), both microscopic and macroscopic effects play an important role. To describe the single-atom response, i.e., the microscopic effects, the semiclassical three-step model has been successfully applied, where in the third step the electron accelerated in the laser field recombines with its parent ion [1,2]. The electron-ion recombination probability strongly decreases both with increasing intensity and with increasing wavelength, which can be attributed to the increased spreading of the continuum electron wave packet [3,4]. For the macroscopic buildup of HHG, a large number of emitters is required. However, the gas density-length product that can be used in HHG is limited by reabsorption of the generated radiation and by phase mismatch [5–7]. To achieve a macroscopically optimized output, careful adjustment of a number of experimental parameters of the HHG medium (type of gas, pressure, medium length, density distribution, etc.) and the driving laser (intensity, focus position, chirp, etc.) [5,8] is required, with an intensity that typically lies in the range of 10^{14}–10^{15} W/cm^2. When generating extreme-ultraviolet (XUV) or soft-x-ray pulses at different photon energies, the conditions to achieve efficient HHG change substantially and typically require different driving laser wavelengths and substantially different gas pressures [7].

In addition to the single-atom response and phase matching, reshaping of the driving laser in the HHG medium has obtained increasing attention. Propagation effects have been exploited, e.g., for the generation of high-flux XUV pulses in loose-focusing geometries [9–11], for the generation of XUV (quasi)continua [12–14], and for the optimization of HHG in the soft-x-ray region [15] up to the water window [16]. Propagation effects have also been exploited to induce or enhance an attosecond lighthouse effect [17–19] and for the generation of isolated attosecond pulses [20]. The studies presented a scheme in Refs. [16,20], in which the driving laser intensity was reduced by a factor up to 3 during propagation through the HHG medium, referred to as the overdriven regime.

Here we report on an unusual HHG scheme that may be described as a strongly overdriven regime. We use conditions where the driving laser is focused to intensities around 10^{16} W/cm^2 (in the absence of the HHG medium) in combination with a high-pressure atomic jet that both reshapes the near-infrared (NIR) pulses and serves as the HHG medium. As a result, a dense plasma is generated which strongly modifies the spatial, spectral, and temporal properties of the NIR driving pulses. Our experimental and numerical results show that ionization-induced self-phase modulation (SPM) and plasma defocusing significantly affect the HHG under these conditions. Self-phase modulation results in a large blueshift and broadening of the driving laser spectrum, while plasma defocusing strongly decreases the NIR intensity at the end of the atomic jet. As a result of both the decreased driving laser intensity and the spectral blueshift, the single-atom response is substantially improved. Furthermore, the scheme benefits from the large number of emitters and good phase-matching

*kkovacs@itim-cj.ro
†bernd.schuette@mbi-berlin.de
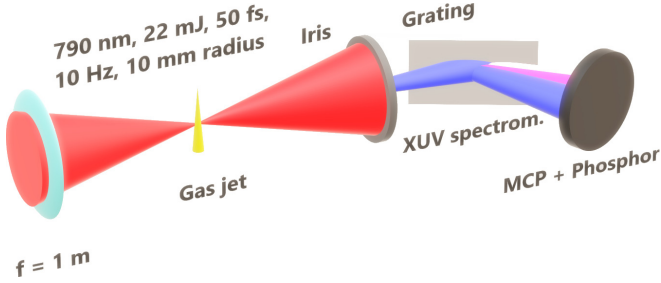
FIG. 1. Schematic of the experimental setup. An NIR beam is focused into a dense atomic jet using a lens with a focal length of 1 m, resulting in an increase of the divergence and a spectral blueshift of the driving pulses. The generated XUV spectrum is analyzed using an XUV spectrometer.

conditions in the second part of the gas medium, as shown by numerical calculations. The process is self-regulating, because reshaping is more pronounced at higher electron densities. As we demonstrate in this work, the scheme works in all atomic gases and enables the generation of XUV and soft-x-ray continua driven by relatively long (50-fs) NIR pulses. An advantage of this concept is moreover that it allows simple switching between different XUV or soft-x-ray spectral regions using different gases, without the need to change the geometry or time-consuming optimization procedures.

II. EXPERIMENTAL SETUP

The experiments were performed at the Max-Born-Institut using a setup (Fig. 1) that is similar to a compact intense XUV setup that we recently demonstrated [21]. Near-infrared pulses (central wavelength of 790 nm, pulse energy up to 22 mJ, pulse duration of 50 fs, and repetition rate of 10 Hz) obtained from a Ti:sapphire amplifier [22] were focused into a gas jet using a spherical lens with a focal length of 1 m. The $1/e^2$ radius of the NIR pulses before focusing was 10 mm and the focused beam waist radius was measured as 42 μm. This leads to a focused NIR peak intensity up to 1.6×10^{16} W/cm^2 in the absence of a gas medium. The atomic jet was generated by a piezoelectric valve with an orifice diameter of 0.5 mm that was placed in the NIR focal plane, and HHG was performed directly at the exit of the nozzle. A backing pressure up to 2 bar was used for Xe and Kr, 4 bar was used for Ar, and 10 bar was used for Ne and He. The pressure in the interaction region is expected to be lower by a factor of at least 5 [23], and the atomic density along the laser propagation direction can be well approximated by a parabolic distribution [24]. Near-infrared spectra were recorded by placing a screen in the NIR beam path inside the vacuum and by recording the scattered light through a vacuum window using an NIR spectrometer. Extreme-ultraviolet spectra were measured by an XUV spectrometer consisting of a diffraction grating and a microchannel plate and phosphor screen assembly.

III. EXPERIMENTAL RESULTS

Figure 2 shows that the NIR driving pulses are substantially broadened and blueshifted after propagation through a dense jet consisting of Xe, Kr, Ar, Ne, or He. In addition to the
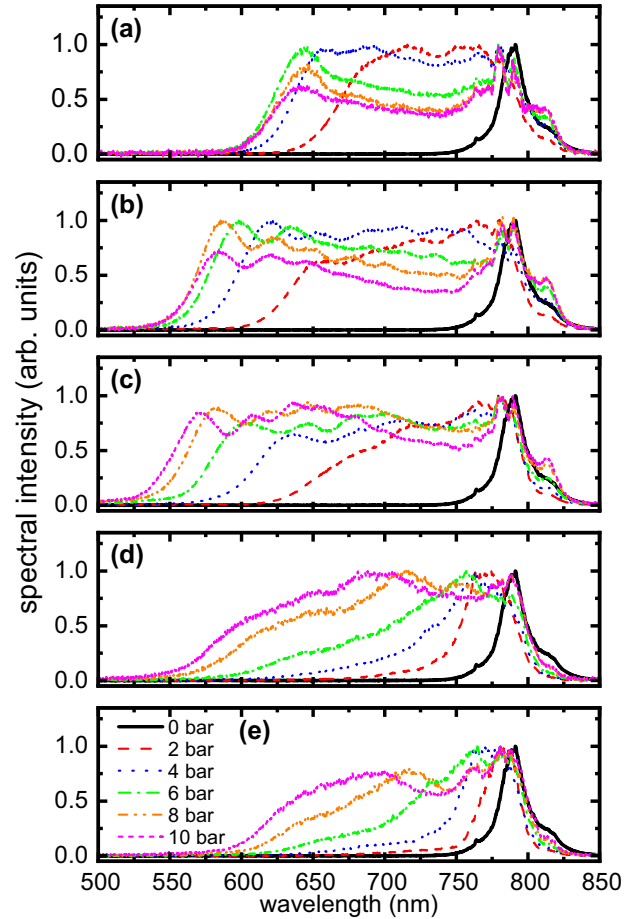
FIG. 2. Spectral broadening of the driving laser pulses for (a) Xe at 5×10^{15} W/cm^2, (b) Kr at 8×10^{15} W/cm^2, (c) Ar at 8×10^{15} W/cm^2, (d) Ne at 1.6×10^{16} W/cm^2, and (e) He at 1.6×10^{16} W/cm^2 using backing pressures from 2 to 10 bar. The spectra are normalized and the applied peak intensities are indicated. The black solid curve corresponds to the unperturbed NIR spectrum.

atomic species, the only parameter that was changed was the NIR pulse energy. Higher pulse energies were used for atomic species with higher ionization potentials to generate sufficiently dense plasmas which are required for efficient reshaping. The NIR peak intensity ranged from 5×10^{15} W/cm^2 for Xe to 1.6×10^{16} W/cm^2 for Ne and He. In the investigated parameter regime, the largest broadening is observed in Ar, where the full width at half maximum is increased from 20 nm to 250 nm using a backing pressure of 10 bar. In the other gases the spectral width is increased by one order of magnitude as well. It is evident that atomic species with higher ionization potentials require higher gas pressures and higher intensities to achieve a similar broadening effect. Moreover, we have observed an increased divergence of the NIR pulses in the presence of the atomic jet. For instance, in the case of Ne using a backing pressure of 10 bar, the divergence of the driving laser was increased by a factor of about 4.

Spatially integrated HHG spectra obtained under the conditions of Fig. 2 are displayed in Fig. 3 for Xe, Kr, Ar, Ne, and He (orange dotted curves). For comparison, HHG
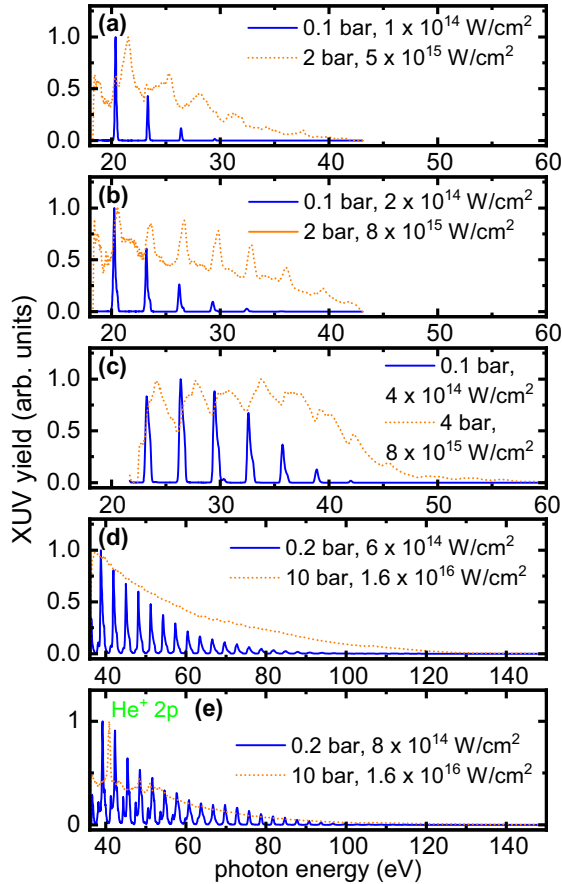
FIG. 3. Normalized HHG spectra obtained from (a) Xe, (b) Kr, (c) Ar, (d) Ne, and (e) He. The blue solid curves represent spectra recorded at standard HHG conditions, i.e., moderate driving laser intensities and gas pressures, resulting in narrowband harmonics. The orange dotted curves represent HHG spectra obtained in the high-pressure jet (2–10 bar) at NIR driving laser intensities of 0.5×10^{16} W/cm² (Xe), 0.8×10^{16} W/cm² (Kr and Ar), and 1.6×10^{16} W/cm² (Ne and He). In (e) narrowband lines are visible within the otherwise continuous HHG spectrum (orange dotted curve), which are attributed to NIR-induced free-induction decay [25] involving the $2p$ and higher excited states of He⁺ ions.

spectra obtained at lower intensities and lower gas densities are shown as well (blue solid curves), where individual narrowband harmonics are clearly discernible. It is evident that when going from a standard HHG regime (blue solid curves) to the strongly overdriven regime (orange dotted curves), the harmonic spectra are substantially broadened. This results in (quasi)continuous XUV and soft-x-ray spectra spanning the range from 18 to 140 eV when using different atomic species. In those cases where individual harmonics are still visible in the strongly overdriven regime [orange dotted curves in Figs. 3(a)–3(c)], clear spectral blueshifts are observed with respect to the harmonics in the standard HHG regime (blue solid curves).

Spatially resolved HHG spectra from Ne using backing pressures of 2 bar (corresponding to an estimated pressure in the interaction zone equal to 400 mbar or less) and 10 bar are presented in Fig. 4. This shows that while some harmonic structure is visible, the spectra are quasicontinuous
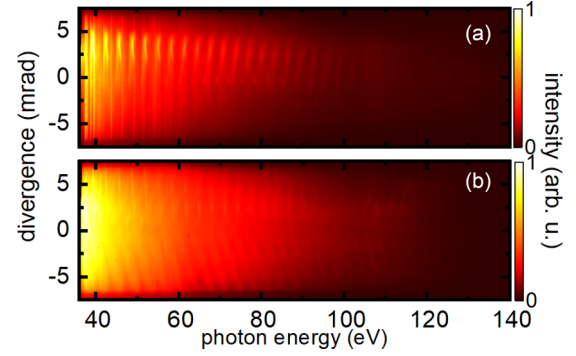
FIG. 4. Spatially resolved HHG spectra for Ne using a backing pressure of (a) 2 bar and (b) 10 bar. The horizontal axis refers to the spectral coordinate and the vertical axis corresponds to the divergence.

independent of the spatial position. It is further evident that the harmonic structure becomes less pronounced with increasing pressure.

The XUV pulse energy is estimated to be about 150 nJ for HHG in Xe and Kr using an XUV photodiode [21]. We note that a comparison of the flux in the two regimes is not meaningful, as HHG in the standard regime was not optimized for flux. In comparison to our flux-optimized HHG scheme [21], the flux in the present work is lower by about a factor of 2. At the same time, both our XUV pulse energy and conversion efficiency are substantially higher than in typical setups, in which hollow-core fiber compression is used to generate continuous XUV spectra (see, e.g., [26,27]).

IV. SIMULATIONS

To understand the physics leading to HHG in the strongly overdriven regime, we have performed extensive numerical calculations in Ne using the adapted version of a three-dimensional nonadiabatic model described in Refs. [28–30]. These calculations took into account the propagation of the driving laser within the atomic jet, the induced atomic dipole response, and the propagation of the harmonic field. Multiple ionization of the atomic species was included [31], which affects the density of free electrons and thereby influences the propagation of the driving pulses. High-order harmonic generation from ions, however, is negligible. Phase matching was calculated using the model described in [32], taking into account the propagated fields as obtained from the solution of the propagation equation [33]. To keep the calculations feasible, we restricted them to an NIR intensity of 8×10^{15} W/cm² and a maximum pressure of 400 mbar. We can therefore expect only qualitative agreement between the experiments and the simulations.

In the first step, we study the reshaping of the driving field, as this is essential to understand the conditions under which HHG takes place. Figure 5(a) shows the radially resolved NIR intensity distribution as a function of the propagation distance z within the atomic jet using a peak pressure of 400 mbar. The NIR peak intensity decreases rapidly during propagation through the jet due to plasma defocusing and absorption, from an initial value of 8×10^{15} W/cm² (black arrow) to a final
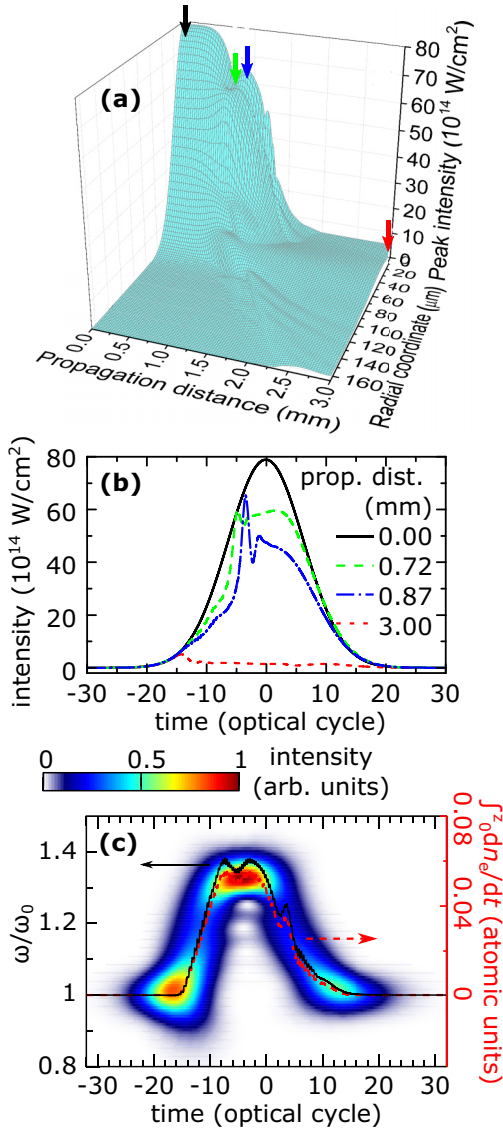
FIG. 5. Simulated properties of NIR pulses with an initial peak intensity of 8×10^{15} W/cm² during and after propagation through a Ne jet using a peak pressure of 400 mbar. (a) Radially resolved NIR intensity distribution as a function of the propagation distance z through the jet. The arrows mark specific z values for which the on-axis temporal intensity distributions are shown in (b). (c) Driving laser spectral properties as a function of time. The black solid curve shows the cycle-averaged carrier frequency (normalized to the initial nominal central frequency) calculated from the temporal change of the refractive index, which is dominated by changes of the density of free electrons n_e (red dashed curve).

FIG. 6. Simulation results showing the spatial evolution of different microscopic and macroscopic quantities in HHG in the spectral region from 42 to 45 eV. (a) Polarizability shown in logarithmic scale for H27, (b) time-dependent coherence length calculated at $t = -12$ optical cycles (o.c.) of the driving laser (in logarithmic scale), and (c) macroscopic buildup of the harmonic signal for H27 intensity (in logarithmic scale). The black solid curve in (c) shows the parabolic pressure distribution which is peaked at 1.5 mm.

value of 5×10^{14} W/cm² (red arrow). At the same time, the beam radius is increased from 45 to 192 μm. We note that for a peak pressure of 133 mbar, a final NIR intensity of 6×10^{14} W/cm² is reached, indicating that the process is self-regulating. The NIR peak intensity does not decrease monotonically as a function of z, but exhibits intermediate maxima and minima, which are exemplarily indicated by the blue and green arrows. Temporal intensity distributions at these positions are depicted in Fig. 5(b), showing that the average on-axis intensity decreases with increasing propagation

distance through the jet. Figure 5(c) shows that the driving laser spectrum is blueshifted starting from about -14 optical cycles, which is attributed to ionization-induced SPM [34,35]. Here the spectral shift resulting from the temporal change of the refractive index (black solid curve; see Ref. [36]) is compared with changes of the free-electron density (red dashed curve), which dominates the change of the refractive index.

Simulation results of the microscopic and macroscopic effects of HHG in the photon energy range from 42 to 45 eV are presented in Fig. 6. The polarizability as a function of the propagation distance and the radial coordinate [Fig. 6(a)] exhibits the highest values around the center of the jet, i.e.,

at 1.5 mm [see black solid curve in Fig. 6(c)], where the density of emitters is highest. In Fig. 6(b) the spatial evolution of the coherence length is presented [calculated at time $t = -12$ optical cycles of the driving laser; cf. Fig. 5(b)]. We consider good phase-matching conditions when the coherence length is comparable to the medium length, which is achieved at propagation distances greater than 1.75 mm. As a result of both microscopic and macroscopic effects, the HHG intensity map [Fig. 6(c)] shows that at larger radii the HHG intensity is highest in the second half of the medium, which is ascribed to a favorable combination of high polarizability and long coherence length. At smaller radii (less than 30 μm) the HHG intensity is peaked around the center of the jet due to the large number of emitters. However, the yield decreases during further propagation through the jet, which is attributed to the short coherence length and in particular to reabsorption of the generated harmonics as a result of the pressure gradient [37]. This suggests that in the future higher HHG conversion efficiencies might be achieved by tailoring the gas jet density profile to have a steep pressure gradient. The results presented in Fig. 6 demonstrate that one advantage of the overdriven regime is the increased volume from which harmonics are generated. Without reshaping of the NIR pulse, the NIR intensity and thus the HHG yield would be negligible at radii greater than 60 μm (note that the volume increases quadratically with the radius).

The XUV spectrum evaluated 70 cm behind the jet [Fig. 7(a)] obtained at a pressure of 133 mbar (red solid curve) shows narrowband harmonics, whereas the spectrum obtained at 400 mbar (blue dotted curve) is quasicontinuous, in qualitative agreement with the experimental results. Note that harmonics are still clearly visible in this simulated spectrum [similar to the experimental spectrum obtained at a backing pressure of 2 bar shown in Fig. 4(a)]. High-order harmonic generation emission in the far field as a function of time and the radial coordinate is shown in Fig. 7(b). On one hand, a contribution is visible at radii less than 0.7 mm, which is peaked around −14 optical cycles, corresponding to the time at which the NIR intensity is highest [cf. Fig. 5(b)]. On the other hand, a contribution appears at larger radii, which around −13 optical cycles starts to be clearly separated from the contribution at small radii. In this regime, the divergence of each consecutive attosecond burst increases, which is reminiscent of the attosecond lighthouse effect [17,38,39]. The bending of the individual attosecond bursts towards larger radii is a result of the wavefront curvature of the XUV beam in the far field. The horizontal lines in Fig. 7(c) indicate that spatial filtering in the far field could be applied to obtain relatively short attosecond pulse trains.

V. CONCLUSION

In this work we have shown that NIR driving laser intensities far above the typical intensities can be used for efficient HHG by exploiting substantial spatial and spectral reshaping of the driving laser in a high-pressure atomic jet. Experimental signatures of this reshaping were a large spectral blueshift and a broadening of both the NIR spectra and the generated harmonics. These results were reproduced by numerical
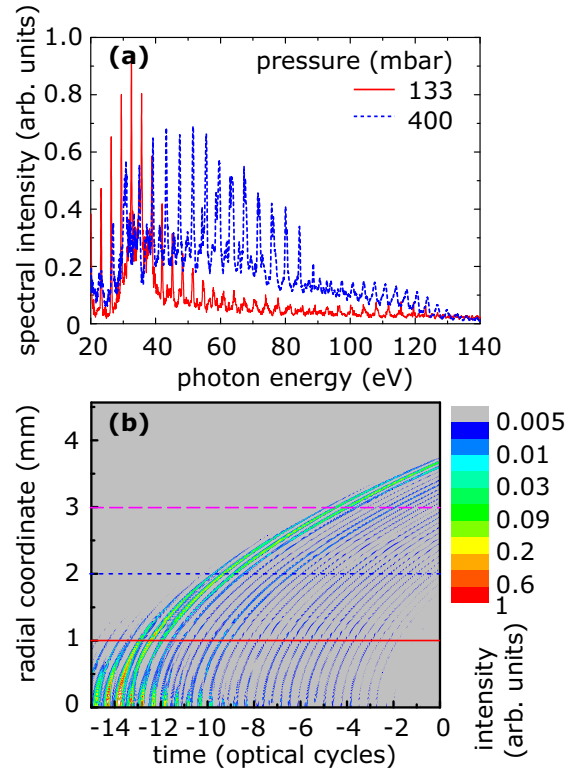
FIG. 7. Simulated HHG properties in the strongly overdriven regime. (a) Spatially integrated HHG spectra at pressures of 133 mbar (red solid curve) and 400 mbar (blue dotted curve), showing the generation of a quasicontinuous XUV spectrum in the latter case. (b) Radially dependent HHG emission for harmonic orders 15–51 as a function of time. The data were analyzed at a distance of 70 cm from the jet and are shown on a logarithmic scale. The horizontal lines indicate that spatial filtering may result in the generation of short attosecond pulse trains.

calculations, which further showed that substantial temporal reshaping takes place in the gas jet. Both experiments and simulations indicated that this is a self-regulating process, where strong reshaping takes place until the plasma density generated by the driving laser becomes sufficiently low to suppress further reshaping, thereby providing good conditions for efficient HHG. As a result, the scheme works in all atomic gases with only a few simple changes of the experimental parameters.

Our approach represents a simple method for the generation of continuous XUV and soft-x-ray spectra by HHG using long driving laser pulses. As such it is ideally suited for transient absorption and reflection spectroscopy in atomic, molecular, and solid-state targets [40]. Furthermore, our results suggest that it is possible to spatially select a short attosecond pulse train. These few-femtosecond XUV pulses might be used in combination with pump-probe techniques in which the temporal resolution is not limited by the pulse duration of the probe laser. One example is terahertz streaking that can be used to resolve few-femtosecond dynamics in spite of the much longer picosecond durations of the terahertz pulses [41].

[1] P. B. Corkum, Phys. Rev. Lett. **71**, 1994 (1993).

[2] M. Lewenstein, P. Balcou, M. Y. Ivanov, A. L'Huillier, and P. B. Corkum, Phys. Rev. A **49**, 2117 (1994).

[3] J. Tate, T. Auguste, H. G. Muller, P. Salières, P. Agostini, and L. F. DiMauro, Phys. Rev. Lett. **98**, 013901 (2007).

[4] A. D. Shiner, C. Trallero-Herrero, N. Kajumba, H.-C. Bandulet, D. Comtois, F. Légaré, M. Giguère, J.-C. Kieffer, P. B. Corkum, and D. M. Villeneuve, Phys. Rev. Lett. **103**, 073902 (2009).

[5] E. Constant, D. Garzella, P. Breger, E. Mével, C. Dorrer, C. Le Blanc, F. Salin, and P. Agostini, Phys. Rev. Lett. **82**, 1668 (1999).

[6] C. Winterfeldt, C. Spielmann, and G. Gerber, Rev. Mod. Phys. **80**, 117 (2008).

[7] T. Popmintchev, M.-C. Chen, D. Popmintchev, P. Arpin, S. Brown, S. Ališauskas, G. Andriukaitis, T. Balčiunas, O. D. Mücke, A. Pugzlys, A. Baltuška, B. Shim, S. E. Schrauth, A. Gaeta, C. Hernández-García, L. Plaja, A. Becker, A. Jaron-Becker, M. M. Murnane, and H. C. Kapteyn, Science **336**, 1287 (2012).

[8] C. M. Heyl, C. L. Arnold, A. Couairon, and A. L'Huillier, J. Phys. B **50**, 013001 (2017).

[9] V. Tosa, E. Takahashi, Y. Nabekawa, and K. Midorikawa, Phys. Rev. A **67**, 063817 (2003).

[10] D. E. Rivas, B. Major, M. Weidman, W. Helml, G. Marcus, R. Kienberger, D. Charalambidis, P. Tzallas, E. Balogh, K. Kovács, V. Tosa, B. Bergues, K. Varjú, and L. Veisz, Optica **5**, 1283 (2018).

[11] B. Major, M. Kretschmar, O. Ghafur, A. Hoffmann, K. Kovács, K. Varjú, B. Senfftleben, J. Tümmler, I. Will, T. Nagy, D. Rupp, M. J. J. Vrakking, V. Tosa, and B. Schütte, J. Phys. Photon. **2**, 034002 (2020).

[12] T. Sekikawa, T. Kumazaki, Y. Kobayashi, Y. Nabekawa, and S. Watanabe, J. Opt. Soc. Am. B **15**, 1406 (1998).

[13] B. Zeng, W. Chu, G. Li, J. Yao, J. Ni, H. Zhang, Y. Cheng, Z. Xu, Y. Wu, and Z. Chang, Phys. Rev. A **85**, 033839 (2012).

[14] A. Dubrouil, O. Hort, F. Catoire, D. Descamps, S. Petit, E. Mével, V. Strelkov, and E. Constant, Nat. Commun. **5**, 4637 (2014).

[15] B. Schütte, P. Weber, K. Kovács, E. Balogh, B. Major, V. Tosa, S. Han, M. J. J. Vrakking, K. Varjú, and A. Rouzée, Opt. Express **23**, 33947 (2015).

[16] A. S. Johnson, D. R. Austin, D. A. Wood, C. Brahms, A. Gregory, K. B. Holzner, S. Jarosch, E. W. Larsen, S. Parker, C. S. Strüber, P. Ye, J. W. G. Tisch, and J. P. Marangos, Sci. Adv. **4**, eaar3761 (2018).

[17] V. Tosa, J. S. Lee, H. T. Kim, and C. H. Nam, Phys. Rev. A **91**, 051801(R) (2015).

[18] E. Balogh, C. Zhang, T. Ruchon, J.-F. Hergott, F. Quere, P. Corkum, C. H. Nam, and K. T. Kim, Optica **4**, 48 (2017).

[19] X. Tang, K. Wang, B. Li, Y. Chen, C. D. Lin, and C. Jin, Opt. Lett. **46**, 5137 (2021).

[20] J. Schötz, B. Förg, W. Schweinberger, I. Liontos, H. A. Masood, A. M. Kamal, C. Jakubeit, N. G. Kling, T. Paasch-Colberg, S. Biswas, M. Högner, I. Pupeza, M. Alharbi, A. M. Azzeer, and M. F. Kling, Phys. Rev. X **10**, 041011 (2020).

[21] B. Major, O. Ghafur, K. Kovács, K. Varjú, V. Tosa, M. J. J. Vrakking, and B. Schütte, Optica **8**, 960 (2021).

[22] G. Gademann, F. Ple, P.-M. Paul, and M. J. J. Vrakking, Opt. Express **19**, 24922 (2011).

[23] L. Drescher, O. Kornilov, T. Witting, V. Shokeen, M. Vrakking, and B. Schütte, Nat. Photon. **15**, 263 (2021).

[24] L. Drescher, O. Kornilov, T. Witting, G. Reitsma, N. Monserud, A. Rouzée, J. Mikosch, M. J. Vrakking, and B. Schütte, Nature (London) **564**, 91 (2018).

[25] S. Beaulieu, S. Camp, D. Descamps, A. Comby, V. Wanie, S. Petit, F. Légaré, K. J. Schafer, M. B. Gaarde, F. Catoire, and Y. Mairesse, Phys. Rev. Lett. **117**, 203001 (2016).

[26] T. Barillot, P. Matia-Hernando, D. Greening, D. Walke, T. Witting, L. Frasinski, J. Marangos, and J. Tisch, Chem. Phys. Lett. **683**, 38 (2017).

[27] T. Witting, M. Osolodkov, F. Schell, F. Morales, S. Patchkovskii, P. Šušnjar, F. H. M. Cavalcante, C. S. Menoni, C. P. Schulz, F. J. Furch, and M. J. J. Vrakking, Optica **9**, 145 (2022).

[28] V. Tosa, H. T. Kim, I. J. Kim, and C. H. Nam, Phys. Rev. A **71**, 063807 (2005).

[29] V. Tosa, H. T. Kim, I. J. Kim, and C. H. Nam, Phys. Rev. A **71**, 063808 (2005).

[30] B. Major, K. Kovács, V. Tosa, P. Rudawski, A. L'Huillier, and K. Varjú, J. Opt. Soc. Am. B **36**, 1594 (2019).

[31] V. Tosa, K. Kovács, B. Major, E. Balogh, and K. Varjú, Quantum Electron. **46**, 321 (2016).

[32] P. Balcou, P. Salières, A. L'Huillier, and M. Lewenstein, Phys. Rev. A **55**, 3204 (1997).

[33] C. Vozzi, M. Negro, F. Calegari, S. Stagira, K. Kovács, and V. Tosa, New J. Phys. **13**, 073003 (2011).

[34] N. Bloembergen, Opt. Commun. **8**, 285 (1973).

[35] Z.-H. He, J. A. Nees, B. Hou, K. Krushelnick, and A. G. R. Thomas, Phys. Rev. Lett. **113**, 263904 (2014).

[36] B. M. Penetrante, J. N. Bardsley, W. M. Wood, C. W. Siders, and M. C. Downer, J. Opt. Soc. Am. B **9**, 2032 (1992).

[37] B. Major and K. Varjú, J. Phys. B **54**, 224002 (2021).

[38] H. Vincenti and F. Quéré, Phys. Rev. Lett. **108**, 113904 (2012).

[39] K. T. Kim, C. Zhang, T. Ruchon, J.-F. Hergott, T. Auguste, D. Villeneuve, P. Corkum, and F. Quéré, Nat. Photon. **7**, 651 (2013).

[40] R. Geneaux, H. J. B. Marroux, A. Guggenmos, D. M. Neumark, and S. R. Leone, Philos. Trans. R. Soc. A **377**, 20170463 (2019).

[41] B. Schütte, S. Bauch, U. Frühling, M. Wieland, M. Gensch, E. Plönjes, T. Gaumnitz, A. Azima, M. Bonitz, and M. Drescher, Phys. Rev. Lett. **108**, 253003 (2012).